

# Search for Majorana neutrinos with the first two years of EXO-200 data

J.B. Albert,<sup>1</sup> D.J. Auty,<sup>2</sup> P.S. Barbeau,<sup>3</sup> E. Beauchamp,<sup>4</sup> D. Beck,<sup>5</sup> V. Belov,<sup>6</sup> C. Benitez-Medina,<sup>7</sup> J. Bonatt,<sup>8,9</sup> M. Breidenbach,<sup>10</sup> T. Brunner,<sup>9</sup> A. Burenkov,<sup>6</sup> G.F. Cao,<sup>11</sup> C. Chambers,<sup>7</sup> J. Chaves,<sup>9</sup> B. Cleveland,<sup>4, a</sup> M. Coon,<sup>5</sup> A. Craycraft,<sup>7</sup> T. Daniels,<sup>8</sup> M. Danilov,<sup>6</sup> S.J. Daugherty,<sup>1</sup> C.G. Davis,<sup>12</sup> J. Davis,<sup>9</sup> R. DeVoe,<sup>9</sup> S. Delaquis,<sup>13</sup> T. Didberidze,<sup>2</sup> A. Dolgolenko,<sup>6</sup> M.J. Dolinski,<sup>14</sup> M. Dunford,<sup>15</sup> W. Fairbank Jr.,<sup>7</sup> J. Farine,<sup>4</sup> W. Feldmeier,<sup>16</sup> P. Fierlinger,<sup>16</sup> D. Fudenberg,<sup>9</sup> G. Giroux,<sup>13, b</sup> R. Gornea,<sup>13</sup> K. Graham,<sup>15</sup> G. Gratta,<sup>9</sup> C. Hall,<sup>12</sup> S. Herrin,<sup>10</sup> M. Hughes,<sup>2</sup> M.J. Jewell,<sup>14</sup> X.S. Jiang,<sup>11</sup> A. Johnson,<sup>10</sup> T.N. Johnson,<sup>1</sup> S. Johnston,<sup>8</sup> A. Karelin,<sup>6</sup> L.J. Kaufman,<sup>1</sup> R. Killick,<sup>15</sup> T. Koffas,<sup>15</sup> S. Kravitz,<sup>9</sup> A. Kuchenkov,<sup>6</sup> K.S. Kumar,<sup>8</sup> D.S. Leonard,<sup>17</sup> F. Leonard,<sup>15</sup> C. Licciardi,<sup>15</sup> Y.H. Lin,<sup>14</sup> R. MacLellan,<sup>10</sup> M.G. Marino,<sup>16, c</sup> B. Mong,<sup>4</sup> D. Moore,<sup>9</sup> R. Nelson,<sup>18</sup> A. Odian,<sup>10</sup> I. Ostrovskiy,<sup>9</sup> C. Ouellet,<sup>15</sup> A. Piepke,<sup>2</sup> A. Pocar,<sup>8</sup> C.Y. Prescott,<sup>10</sup> A. Rivas,<sup>9</sup> P.C. Rowson,<sup>10</sup> M.P. Rozo,<sup>15</sup> J.J. Russell,<sup>10</sup> A. Schubert,<sup>9</sup> D. Sinclair,<sup>15, 19</sup> S. Slutsky,<sup>12, d</sup> E. Smith,<sup>14</sup> V. Stekhanov,<sup>6</sup> M. Tarka,<sup>5</sup> T. Tolba,<sup>13</sup> D. Tosi,<sup>9, e</sup> K. Twelker,<sup>9</sup> P. Vogel,<sup>20</sup> J.-L. Vuilleumier,<sup>13</sup> A. Waite,<sup>10</sup> J. Walton,<sup>5</sup> T. Walton,<sup>7</sup> M. Weber,<sup>9</sup> L.J. Wen,<sup>11</sup> U. Wichoski,<sup>4</sup> J.D. Wright,<sup>8</sup> L. Yang,<sup>5</sup> Y.-R. Yen,<sup>12, 14</sup> O.Ya. Zeldovich,<sup>6</sup> and Y.B. Zhao<sup>11</sup>

(EXO-200 Collaboration)

<sup>1</sup>*Physics Department and CEEM, Indiana University, Bloomington IN, USA*

<sup>2</sup>*Department of Physics and Astronomy, University of Alabama, Tuscaloosa AL, USA*

<sup>3</sup>*Department of Physics, Duke University, and Triangle Universities Nuclear Laboratory (TUNL), Durham, North Carolina, USA*

<sup>4</sup>*Department of Physics, Laurentian University, Sudbury ON, Canada*

<sup>5</sup>*Physics Department, University of Illinois, Urbana-Champaign IL, USA*

<sup>6</sup>*Institute for Theoretical and Experimental Physics, Moscow, Russia*

<sup>7</sup>*Physics Department, Colorado State University, Fort Collins CO, USA*

<sup>8</sup>*Physics Department, University of Massachusetts, Amherst MA, USA*

<sup>9</sup>*Physics Department, Stanford University, Stanford CA, USA*

<sup>10</sup>*SLAC National Accelerator Laboratory, Stanford CA, USA*

<sup>11</sup>*Institute of High Energy Physics, Beijing, China*

<sup>12</sup>*Physics Department, University of Maryland, College Park MD, USA*

<sup>13</sup>*LHEP, Albert Einstein Center, University of Bern, Bern, Switzerland*

<sup>14</sup>*Department of Physics, Drexel University, Philadelphia PA, USA*

<sup>15</sup>*Physics Department, Carleton University, Ottawa ON, Canada*

<sup>16</sup>*Technische Universität München, Physikdepartment and Excellence Cluster Universe, Garching, Germany*

<sup>17</sup>*Department of Physics, University of Seoul, Seoul, Korea*

<sup>18</sup>*Waste Isolation Pilot Plant, Carlsbad NM, USA*

<sup>19</sup>*TRIUMF, Vancouver, BC, Canada*

<sup>20</sup>*Kellogg Lab, Caltech, Pasadena, CA, USA*

(Dated: June 6, 2014)

Many extensions of the Standard Model of particle physics suggest that neutrinos should be Majorana-type fermions, but this assumption is difficult to confirm. Observation of neutrinoless double-beta decay ( $0\nu\beta\beta$ ), a spontaneous transition that may occur in several candidate nuclei, would verify the Majorana nature of the neutrino and constrain the absolute scale of the neutrino mass spectrum. Recent searches carried out with  $^{76}\text{Ge}$  (GERDA experiment) and  $^{136}\text{Xe}$  (KamLAND-Zen and EXO-200 experiments) have established the lifetime of this decay to be longer than  $10^{25}$  yr, corresponding to a limit on the neutrino mass of 0.2–0.4 eV. Here we report new results from EXO-200 based on 100 kg·yr of  $^{136}\text{Xe}$  exposure, representing an almost fourfold increase from our earlier published datasets. We have improved the detector resolution at the  $^{136}\text{Xe}$  double-beta-decay Q-value to  $\sigma/E = 1.53\%$  and revised the data analysis. The obtained half-life sensitivity is  $1.9 \cdot 10^{25}$  yr, an improvement by a factor of 2.7 compared to previous EXO-200 results. We find no statistically significant evidence for  $0\nu\beta\beta$  decay and set a half-life limit of  $1.1 \cdot 10^{25}$  yr at 90% CL. The high sensitivity holds promise for further running of the EXO-200 detector and future  $0\nu\beta\beta$  decay searches with nEXO.

<sup>a</sup> Also SNOLAB, Sudbury ON, Canada

<sup>b</sup> Now at Queen's University, Kingston, ON, Canada

<sup>c</sup> Corresponding author: michael.marino@mytum.de

<sup>d</sup> Now at California Institute of Technology, Pasadena, CA, USA

<sup>e</sup> Now at University of Wisconsin, Madison, WI, USA

Majorana fermions, a class of neutral spin-1/2 particles described by 2-component spinors, have been an element of quantum field theory since its inception [1, 2]. Electrons and other spin-1/2 elementary particles with distinct antiparticles, however, are described by 4-component Dirac spinors. Majorana quasiparticles may have been observed in condensed matter systems [3] where neutrality is achieved through the collective action of electrons and holes. Among the known *elementary* particles, only neutrinos are Majorana fermion candidates, owing to their intrinsic neutrality. Confirmation of this property would imply the non-conservation of lepton number, an additive quantum number that, unlike charge or color, is not related to any known gauge symmetry. As yet, lepton number has been empirically found to be conserved. Neutrinos are also remarkable for their small, yet finite, masses [4] that are generally difficult to explain, but arise naturally in many extensions [5, 6] of the Standard Model of particle physics (SM). A generic consequence of many such extensions is that neutrinos should be of the Majorana variety.

The most sensitive probe for Majorana neutrinos is a nuclear process known as neutrinoless double-beta decay ( $0\nu\beta\beta$ ), whereby a nucleus decays by emitting two electrons and nothing else, while changing its charge by two units [7]. A related double-beta decay process, known as two-neutrino double-beta decay ( $2\nu\beta\beta$ ), is allowed by the SM and has been observed in many nuclei,  $^{136}\text{Xe}$  among them [8, 9]. It provides, however, no direct information on the Majorana/Dirac question. The exotic  $0\nu\beta\beta$  can be distinguished from the  $2\nu\beta\beta$  by measuring the sum energy of the two electrons that is peaked at the Q-value for the former and is a continuum for the latter. We refer to this region around the Q-value as the  $0\nu\beta\beta$  region-of-interest (ROI). The half-life of the  $0\nu\beta\beta$  is related to the effective Majorana neutrino mass ( $\langle m_{\beta\beta} \rangle$ ) by a phase space factor and a nuclear matrix element. Hence the observation of the  $0\nu\beta\beta$  decay would discover elementary Majorana particles, demonstrate lepton number violation and measure the neutrino mass scale  $\langle m_{\beta\beta} \rangle$ , at least to within the theoretical uncertainty of the nuclear matrix elements [10].

Recent sensitive searches for  $0\nu\beta\beta$  have been carried out in  $^{76}\text{Ge}$  (GERDA [11]) and  $^{136}\text{Xe}$  (KamLAND-Zen [12] and EXO-200 [13]). These experiments have set limits on the Majorana neutrino mass of  $\sim 0.2\text{--}0.4$  eV, and have cast doubt on an earlier claim of observation [14]. In this letter we report on new  $0\nu\beta\beta$  search results from the EXO-200 experiment based upon about two years of data.

## I. EXO-200 DETECTOR

EXO-200 has been described in detail elsewhere [15]. Briefly, the detector is a cylindrical liquid xenon (LXe) time projection chamber (TPC), roughly 40 cm in diameter and 44 cm in length. Two drift regions are

separated in the center by a cathode. The LXe is enriched to 80.6% in  $^{136}\text{Xe}$ , the  $0\nu\beta\beta$  candidate ( $Q = 2457.83 \pm 0.37$  keV [16]). The TPC provides X-Y-Z coordinate and energy measurements of ionization deposits in the LXe by simultaneously collecting the scintillation light and the charge. Charge deposits spatially separated by about 1 cm or more are individually observed and the position accuracy for isolated deposits is a few mm. Avalanche Photodiodes (APDs) measure the scintillation light. Small radioactive sources can be positioned at standard positions near the TPC to calibrate the detector and monitor its stability.

The TPC is shielded from environmental radioactivity on all sides by  $\sim 50$  cm of HFE-7000 cryofluid [17] (HFE) maintained at  $\sim 167$  K inside a vacuum-insulated copper cryostat. Further shielding is provided by at least 25 cm of lead in all directions. The entire assembly is housed in a cleanroom located underground at a depth of  $1585^{+11}_-6$  meters water equivalent [18] at the Waste Isolation Pilot Plant near Carlsbad, NM, USA. Four of the six sides of the cleanroom are instrumented with plastic scintillator panels recording the passage of cosmic ray muons. An extensive materials screening campaign [19] was employed to minimize the radioactive background produced by the detector components.

## II. DATA ANALYSIS AND METHODOLOGY

The data analysis methods in this work follow closely those presented in detail in [9]. Events in the detector are classified as single-site (SS) or multi-site (MS) according to the number of detected charge deposits.  $0\nu\beta\beta$  events are predominantly SS whereas  $\gamma$  backgrounds are mostly MS. For each event, the energy is determined as a linear combination of charge and scintillation, while a ‘standoff distance’ (SD) is defined as the distance between a charge deposit and the closest material that is not LXe, other than the cathode. To search for  $0\nu\beta\beta$ , a binned maximum-likelihood (ML) fit is performed simultaneously over the SS and MS events using probability density functions (PDFs) in energy and SD, generated using a Geant4-based [20] Monte Carlo simulation (MC). The energy range 980–9800 keV is used. The ‘low-background data set’ (physics data) is obtained after applying event selection cuts. With respect to Ref. [9] the current analysis additionally includes: (1) improved signal processing for the scintillation waveforms resulting in lower noise; (2)  $^{226}\text{Ra}$  source calibration data; (3) an expanded fiducial volume; (4) the estimation of systematic errors related to the  $0\nu\beta\beta$  ROI; and (5) updated background and systematic studies relevant to the  $0\nu\beta\beta$  search.

The data set presented here (Run 2) combines Run 2a (already used for [9, 13], September 22, 2011 – April 15, 2012) and Runs 2b and 2c (April 16, 2012 – September 1, 2013). After removing periods of poor data quality and calibration runs, the total amount of low-background

data for this analysis is  $477.60 \pm 0.01$  days, a 3.8-fold increase from previous EXO-200 publications. The primary tool used for understanding and correcting the detector energy measurement is the 2615 keV  $\gamma$  line of  $^{208}\text{Tl}$  from a  $^{228}\text{Th}$  source deployed at least twice weekly during the time spanned by this data set. Seven multi-day calibration campaigns involving the use of multiple sources ( $^{228}\text{Th}$ ,  $^{60}\text{Co}$ ,  $^{226}\text{Ra}$  and  $^{137}\text{Cs}$ ) were performed at roughly 3-month intervals throughout the data set. The lifetime of ionization electrons in the LXe is better than 2 ms for the entire data set, more than sufficient to collect charge across the full volume of the detector. We determine the optimal linear combination of scintillation and ionization signals once per week by minimizing the width of the 2615 keV line. To prevent making analysis decisions that could bias the results in the ROI, the low-background data were partially “masked” to hide  $\sim 2/3$  of the live-time for SS events between 2325 and 2550 keV. Live-time already analyzed in previous publications (e.g. Run 2a) was not masked.

The energy resolution of the detector is dominated by electronic noise in the scintillation readout and exhibits variations over time due to changes in this noise. We apply a denoising algorithm to the scintillation signals during post processing, improving the detector resolution and reducing its time dependence. This algorithm attempts to find the optimal combination of APD waveforms to determine the amount of scintillation light for each event, taking into account the measured electronic noise of each APD channel as well as the position of each charge deposition in the detector. Figure 1 shows the resolution with and without denoising.

We define an effective, time-independent energy resolution function [9]  $\sigma^2(E) = \sigma_{\text{elec}}^2 + b^2E + c^2E^2$ . Here,  $\sigma_{\text{elec}}$ ,  $b$  and  $c$  are 20.8 keV,  $0.628 \text{ keV}^{1/2}$  and  $1.10 \cdot 10^{-3}$  ( $25.8 \text{ keV}$ ,  $0.602 \text{ keV}^{1/2}$  and  $4.04 \cdot 10^{-3}$ ) for SS (MS), determined by a ML fit to calibration data taken during Run 2. This function is folded with the energy distributions derived from the simulation to create the PDFs used in final fits. The effective resolution ( $\sigma/E$ ) for SS (MS) at the  $0\nu\beta\beta$  Q-value is  $1.53 \pm 0.06\%$  ( $1.65 \pm 0.05\%$ ).

The fiducial volume (FV) is larger than in [9] to maximize the sensitive mass while maintaining systematic uncertainties at an acceptable level. Events in the FV are required to have  $182 \text{ mm} > |Z| > 10 \text{ mm}$  (where  $Z = 0$  is the cathode plane) and are contained in a hexagon with 162 mm apothem. This represents a  $^{136}\text{Xe}$  mass of 76.5 kg, corresponding to  $3.39 \times 10^{26}$  atoms of  $^{136}\text{Xe}$  and, with the quoted live-time, results in an exposure of 100 kg·yr (736 mol·yr).

### III. INVESTIGATION AND DETERMINATION OF SYSTEMATIC ERRORS

The main systematic uncertainties relevant to the search for  $0\nu\beta\beta$  are related to (1) signal efficiency, (2) location of the  $0\nu\beta\beta$  ROI within the spectrum, and (3) es-

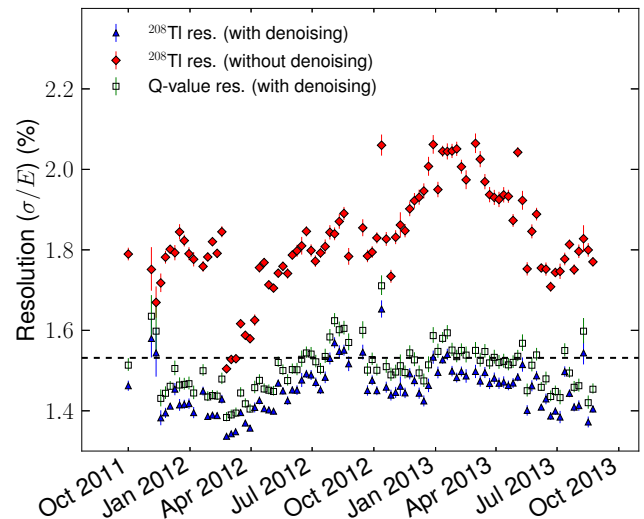


FIG. 1. **Effect of denoising on the energy resolution ( $\sigma/E$ ).** Resolution for SS events versus time with and without application of the denoising algorithm. Shown are resolutions at the 2615 keV  $^{208}\text{Tl}$  full-absorption peak (with and without) and propagated to the  $0\nu\beta\beta$  Q-value (with). The time variation is caused by changes in the noise of the APD front-end electronics. The horizontal dashed line shows the effective Q-value SS energy resolution used for the data set (1.53%). MS resolution (not shown) exhibits similar behavior. The error bars represent  $\pm 1$  standard deviation intervals.

timization of the background in the ROI.

To verify the simulation’s ability to model efficiencies and the background, we compare measurement and simulation of calibration sources deployed at various positions around the TPC, investigating in particular: (a) the energy and SD distributions, (b) the integrated rate of selected events, and (c) the SS/MS event ratio versus energy. A representative set of results for (a) is shown in Fig. 2, where simulation-data agreement for the  $^{226}\text{Ra}$  source are presented.  $^{226}\text{Ra}$  is a particularly valuable source because of several  $\gamma$  lines that map a broad energy region including the  $0\nu\beta\beta$  ROI. The energy spectrum shows good agreement across the energy range of the analysis. Comparable results were also obtained with the  $^{60}\text{Co}$  and  $^{228}\text{Th}$  sources. The SD agreement is within statistical errors except in the first 10 mm bin, where the simulation produces more events in the FV than seen in data.

Discrepancies in the shapes of energy and SD distributions between data and simulation affect the estimation of the background in the  $0\nu\beta\beta$  ROI. To quantify this effect, we calculate skewing functions based upon the small discrepancies observed in source calibration studies. We distort the background PDFs with the skewing functions and use these to produce a set of toy MC data sets. The toy MC data sets are then fit to un-skewed PDFs. The change in the  $0\nu\beta\beta$  ROI background is 9.2%, which we take as systematic error.

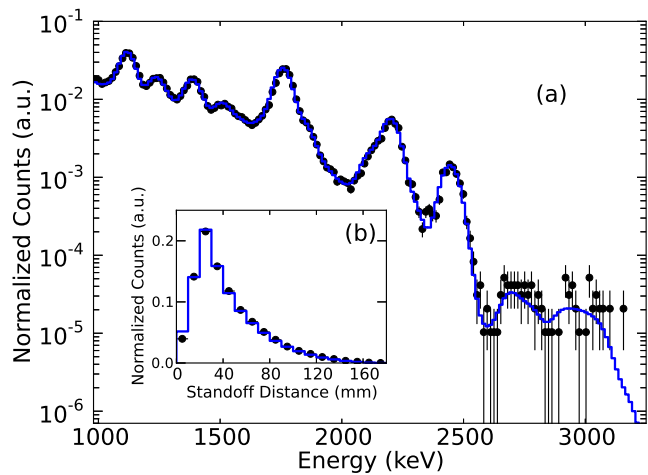


FIG. 2. Comparison of energy and SD distributions of a  $^{226}\text{Ra}$  calibration source for simulation and data. Energy (a) and SD (b) are shown for data (black points) and simulation (blue line). The calibration source is at a position near the cathode outside the TPC. The error bars represent  $\pm 1$  standard deviation intervals.

In the rate comparison studies (b), we combine the total number of selected events in data and simulation as  $(\text{Data} - \text{MC})/\text{Data}$  for several source positions. The error-weighted average of the results is calculated using the FV in this analysis as well as the FV in [9]. The difference between these values is 1.7%, which we combine with the underlying FV uncertainty (also 1.7%, [9]) conservatively assuming full correlation to produce a total error on the detector efficiency of 3.4%.

The ratio of the number of SS events to the total number of events ( $\text{SS}/(\text{SS}+\text{MS})$ ) is compared between data and simulation for three sources in Fig. 3. The general behavior is largely independent of the underlying spectral shape. We choose to assign a single systematic uncertainty to the  $\text{SS}/(\text{SS}+\text{MS})$  ratio of 9.6%, calculated from the weighted average of the maximum deviations observed for the  $^{228}\text{Th}$ ,  $^{60}\text{Co}$  and  $^{226}\text{Ra}$  (data from the latter available after June 2013) sources at several different source locations in each calibration campaign.

Event selection requires an event to be fully reconstructed in all 3 coordinates (X, Y and Z). We compare the relative efficiency of this requirement for  $2\nu\beta\beta$  from MC to the measured relative efficiency derived from the background-subtracted low-background energy spectrum. Here, we define the relative efficiency as the ratio of the number of events passing the entire set of selection requirements to the number passing the set *not including* the full-reconstruction requirement. The relative efficiency from simulation changes modestly across the  $2\nu\beta\beta$  energy range ( $> 99\%$  to  $90\%$  from 980 keV to 2450 keV) and similar behavior is seen in data. The average deviation between simulation and data over the  $2\nu\beta\beta$  spectrum (7.8%) is taken as a systematic error on the efficiency.

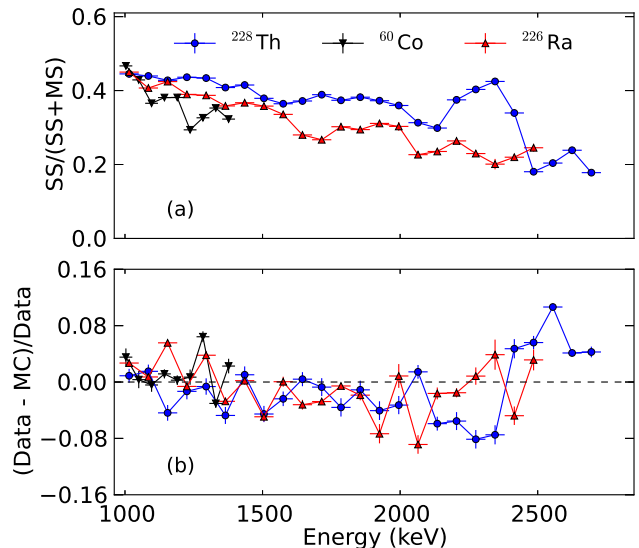


FIG. 3. Event multiplicity in data and simulation. (a)  $\text{SS}/(\text{SS}+\text{MS})$  ratio in data for  $^{226}\text{Ra}$ ,  $^{60}\text{Co}$  and  $^{228}\text{Th}$  calibration sources. (b) Comparison of  $\text{SS}/(\text{SS}+\text{MS})$  ratio between data and simulation for the three sources. Despite having different underlying energy spectra, all sources exhibit similar behavior across the shown energy range when comparing data and simulation (b). The error bars represent  $\pm 1$  standard deviation intervals.

The uncertainty on the location of the ROI in the spectrum is dominated by a possible energy-scale difference between  $\beta$ -like events in the LXe (e.g.  $0\nu\beta\beta$ ) and  $\gamma$ -like events (including most backgrounds and the sources used for the primary energy calibration). We define the ‘ $\beta$ -scale’ as  $E_\beta = B \cdot E_\gamma$ , where  $E_\beta$  ( $E_\gamma$ ) is the energy for depositions from  $\beta$ s ( $\gamma$ s) and  $B$  is a measured constant. We determine the  $\beta$ -scale by fitting to the  $2\nu\beta\beta$ -decay-dominated low-background data and find  $B = 0.999 \pm 0.002$ .

Several cross checks were performed to search for energy dependence in the  $\beta$ -scale. The above fits were performed using different energy thresholds and with different background PDFs produced using the skewing functions discussed earlier. We also fit the low-background data assuming a linear energy dependence (e.g.  $p_0 + p_1 E_\gamma$ ) for  $B$ . In all cases the results are consistent with the original fit, providing no evidence for energy dependence of the  $\beta$ -scale. The estimate of the  $\beta$ -scale is also robust against a different choice of  $2\nu\beta\beta$  spectral shape [21].

To investigate the dependence of the ROI background estimate on the completeness of the fit model, we derive PDFs from different source locations and introduce them separately into the default background model used in the fit. The relative change of the estimated ROI background is then determined. The three background PDFs considered in this study are  $^{238}\text{U}$  in the HFE and inner cryostat, and  $^{60}\text{Co}$  in the copper source guide tube. These were chosen because the initial source location affects relative

Source	Signal eff. (%)	Error (%)
Event selections		
Summary from [9]	93.1	0.9
Partial reconstruction	90.9	7.8
Fiducial Volume/Rate agreement	-	3.4
Total	84.6	8.6

TABLE I.  $0\nu\beta\beta$  signal efficiency and associated systematic errors. ‘Partial reconstruction’ refers to the requirement that all events be fully reconstructed in X,Y and Z. The summary for event selection from [9] includes all efficiencies and related errors except fiducial volume and partial reconstruction, which have been recalculated in this work for  $0\nu\beta\beta$ .

Source	Error (%)
Background shape distortion	9.2
Background model	5.7
Energy resolution variation	1.5
Total	10.9

TABLE II. Systematic errors on the determination of background in the ROI. These arise from incorrect modeling of the background shape (Background shape distortion), incorrect or incomplete background model (Background model), and the residual variation of the energy resolution over time (Energy resolution variation, see e.g. Fig. 1).

amplitudes and spectral features in the ROI, i.e. the  $^{214}\text{Bi}$   $\gamma$  (2448 keV) and  $^{60}\text{Co}$  sum peak. This study indicates a total possible deviation of 5.7% for the expected background counts in the ROI.

The residual time dependence of the energy resolution (Fig. 1) can introduce additional counts in the ROI from the 2615 keV  $^{208}\text{Tl}$  peak. This was estimated to affect the ROI background counts by  $\pm 1.5\%$ .

A summary of the  $0\nu\beta\beta$  signal efficiency and associated uncertainty is presented in Table I. Table II summarizes the uncertainties on the estimation of background in the ROI. These errors are explicitly included as input to the final fit to the low-background data. Items not listed in the tables, such as the  $\beta$ -scale and the SS/MS ratios, still contribute to the total systematic error on the  $0\nu\beta\beta$  signal as they are propagated to the final result by the ML fit to the low-background data.

Neutrons arising from cosmic-ray muons or radioactive decays in the salt surrounding the laboratory may contribute background to the  $0\nu\beta\beta$  ROI via neutron capture or spallation processes. The contribution in the ROI is expected to arise primarily from neutron-capture  $\gamma$ s in the LXe and surrounding materials (e.g. capture on  $^{63}\text{Cu}$  and  $^{65}\text{Cu}$  in the copper components, and on  $^{136}\text{Xe}$  in the LXe). A simulation using a simplified experimen-

tal geometry and employing the FLUKA [22, 23] and SOURCES [24] software packages is used to generate neutrons, track and thermalize them. The resulting neutron capture rates are used as input to the Geant4-based [20] EXO-200 simulation package [9], with the respective n-capture  $\gamma$ -spectra produced based upon ENSDF information [25] for the given nuclides. The produced PDFs are used in fits to the low-background data. Good shape agreement is found between these PDFs and data coincident with muon-veto-panel events.

## IV. RESULTS

The fit to the low-background data minimizes the negative log-likelihood function constructed using a signal and background model composed of PDFs from simulation. A profile-likelihood (PL) scan is performed to search for a  $0\nu\beta\beta$  signal.

The PDFs chosen for the low-background fit model are those used in [9] plus a ‘‘far-source’’  $^{232}\text{Th}$  PDF, a  $^{137}\text{Xe}$  PDF and neutron-capture-related PDFs, including  $^{136}\text{Xe}$  neutron capture in the LXe,  $^1\text{H}$  neutron-capture in the HFE, and  $^{63}\text{Cu}$ ,  $^{65}\text{Cu}$  neutron capture in Cu components (LXe vessel, inner and outer cryostats). The far-source  $^{232}\text{Th}$  PDF allows for background contributions from Th in materials far from the TPC, for example in the HFE and in the copper cryostat. (Remote  $^{238}\text{U}$  is included in the fit model via  $^{222}\text{Rn}$ , simulated in the air between the cryostat and Pb shield.) We combine the neutron-capture-related PDFs to form one PDF, allowing the relative rates of the component PDFs to float within 20% of their simulation-estimated values. The total rate of this summed PDF is allowed to float unconstrained.

We constrain the single-site fractions (SS/(SS+MS)) of all components to be within 9.6% of their value calculated from simulation. An additional 90% correlation between single-site fractions of  $\gamma$  components is introduced into the likelihood function, owing to the consistent behavior observed in these parameters in calibration studies (e.g. Fig. 3). The overall normalization is allowed to float within the estimated systematics errors (8.6%). The background-PDF amplitudes *within* the ROI are also allowed to vary within their estimated systematic error (10.9%). The  $\beta$ -scale is not allowed to float during the fit, but is manually profiled while performing the PL scan for  $0\nu\beta\beta$ .

The final step before performing the fit was the unmasking of live-time around the SS ROI. However, before unmasking the full data set, we investigated backgrounds associated with Xe feeds, irregular occurrences in which additional Xe gas is introduced into the purification circulation loop. (These Xe feeds occurred 10 times over the run period and are known to temporarily elevate, for example, Rn levels in the detector.) The live-time in the two-week periods following the 10 feed events were unmasked first to search for increased background levels in the ROI. No evidence for such an increase was found and

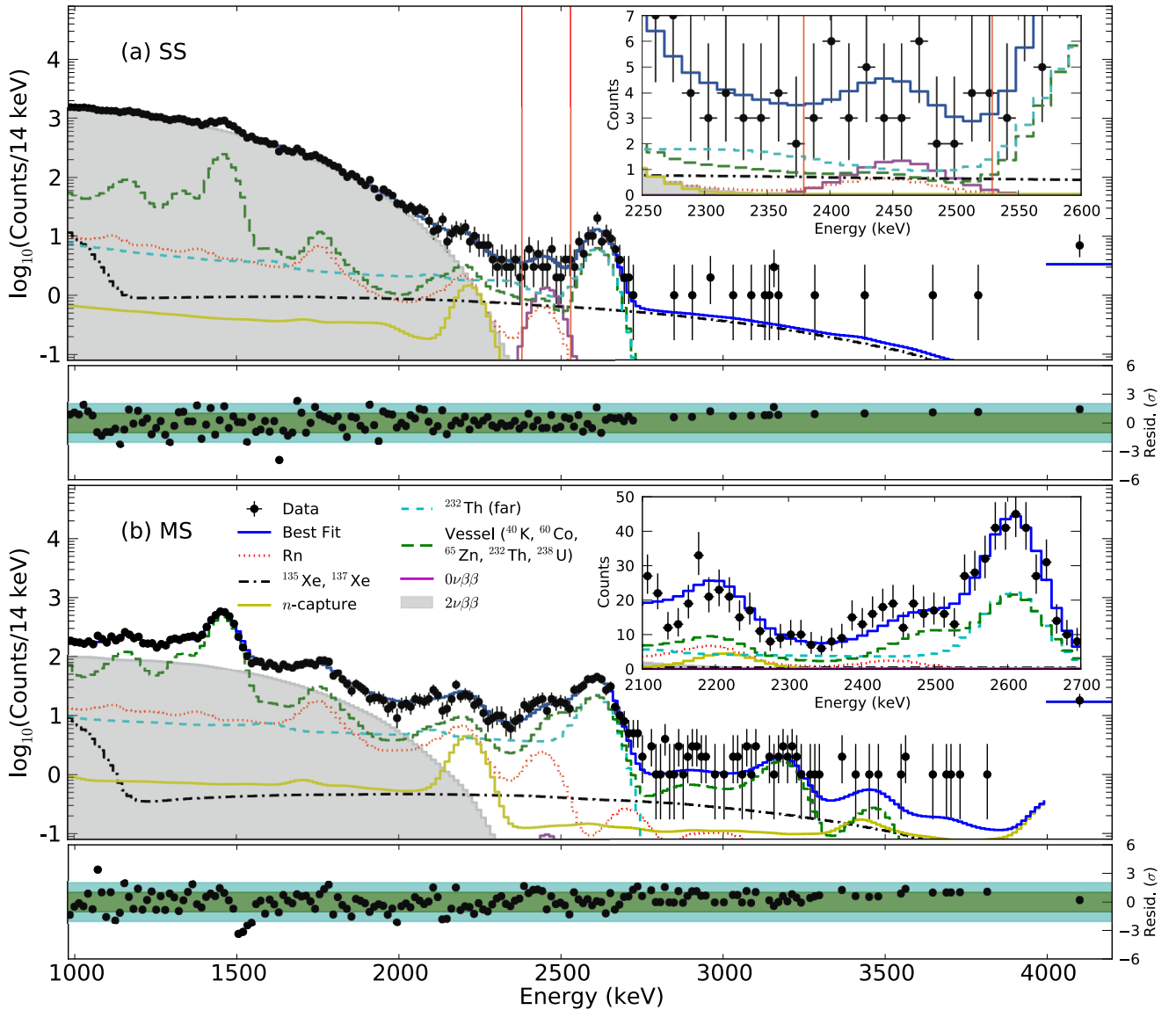


FIG. 4. **Fit results projected in energy.** SS (a) and MS (b) events are shown with a zoom-in (inset) around the ROI region: 2250–2600 keV (2100–2700 keV) for SS (MS). The bin size is 14 keV. Data points are shown in black and residuals between data and best fit normalized to the Poisson error are presented, ignoring bins with 0 events. The 7 (18) events between 4000 and 9800 keV in the SS (MS) spectrum have been collected into an overflow bin for presentation here. The vertical (red) lines in the SS spectra indicate the  $\pm 2\sigma$  ROI. The result of the simultaneous fit to the SD is not shown here. Several background model components, including Rn,  $^{135}\text{Xe}$  and  $^{137}\text{Xe}$ ,  $n$ -capture,  $^{232}\text{Th}$  (far); Vessel;  $0\nu\beta\beta$ ; and  $2\nu\beta\beta$  (described further in the text), are indicated in main panel (b) to show their relative contributions to the spectra. The error bars on the data points represent  $\pm 1$  standard deviation intervals.

the unmasking of the remaining live-time proceeded.

The results of the ML fit are presented in Fig. 4. The measured  $2\nu\beta\beta$  decay rate is consistent with [9]. From the best-fit model, the estimate of the background in the  $0\nu\beta\beta \pm 2\sigma$  ROI is  $31.1 \pm 1.8(\text{stat}) \pm 3.3(\text{sys})$  counts, or  $(1.7 \pm 0.2) \cdot 10^{-3} \text{ keV}^{-1} \text{ kg}^{-1} \text{ yr}^{-1}$  normalized to the *total* Xe exposure (123.7 kg.yr). Both this and the  $\pm 1\sigma$  value (also  $(1.7 \pm 0.2) \cdot 10^{-3} \text{ keV}^{-1} \text{ kg}^{-1} \text{ yr}^{-1}$ ) are consistent with previous results,  $1.5 \pm 0.1$  ( $1.4 \pm 0.1$ ) with the same units in the  $\pm 1\sigma$  ( $\pm 2\sigma$ ) ROI [13]. The dominant

backgrounds arise from  $^{232}\text{Th}$  (16.0 counts),  $^{238}\text{U}$  (8.1 counts) and  $^{137}\text{Xe}$  (7.0 counts). This amount of  $^{137}\text{Xe}$  is consistent with estimates from studies of the activation of  $^{136}\text{Xe}$  in muon-veto-tagged data. The total number of events seen in this region is 39. The best-fit value of  $0\nu\beta\beta$  counts is 9.9, consistent with the null hypothesis at  $1.2\sigma$  as calculated using toy Monte Carlo studies. The corresponding PL scan of this parameter is shown in Fig. 5.

A number of cross checks were performed on the re-

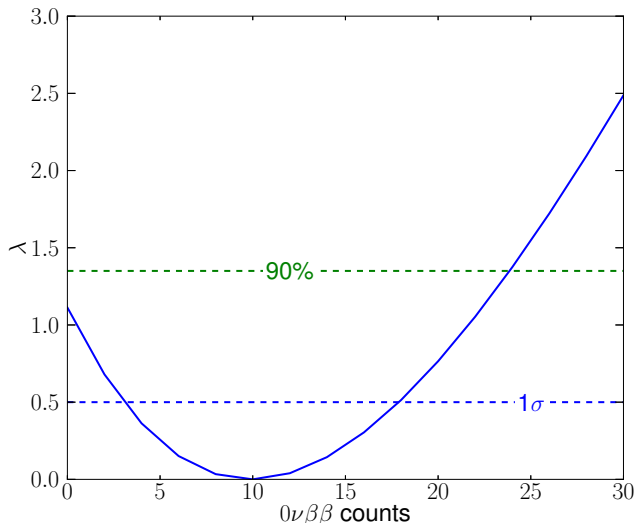


FIG. 5. **Profile likelihood,  $\lambda$ , for  $0\nu\beta\beta$  counts.** The horizontal dashed lines represent the  $1\sigma$  and 90% confidence levels assuming the validity of Wilks’ theorem [26, 27], intersecting the profile curve at (3.1, 18) and 24  $0\nu\beta\beta$  counts, respectively. From toy Monte Carlo studies, the best-fit value is consistent with the null hypothesis at  $1.2\sigma$ .

sult. No event reconstruction anomalies were found after hand-scanning all events in the ROI. The time-between-events distribution of the ROI events is consistent with a constant-rate process and the SD distribution of events in data is consistent with the best-fit model. Additional backgrounds were considered that could contribute events to the ROI. In particular, we tested for  $^{110m}\text{Ag}$  and  $^{88}\text{Y}$  because of their possible association with the measurement in [12], and found that both produce a distinct high-multiplicity signature in EXO-200 (SS/(SS+MS)~5-10%). Separate fits including each of these PDFs contributed the following counts to the  $\pm 2\sigma$  ROI:  $N_{^{110m}\text{Ag}} = 0.04 \pm 0.02$  and  $N_{^{88}\text{Y}} = 0.02 \pm 0.01$ . Finally, we were able to exclude any significant effect on the ROI background from  $^{214}\text{Bi}$  external to the Pb shield, e.g. from  $^{238}\text{U}$  in the surrounding salt.

## V. DISCUSSION

In summary, we report a 90% C.L. lower limit on the  $0\nu\beta\beta$  half-life of  $1.1 \cdot 10^{25}$  yr. With the nuclear matrix elements of [28–31] and phase space factor from [21], this corresponds to an upper limit on the Majorana neutrino mass of 190–450 meV. Using the three flavor fit of [32] (with private communication, M. Tortola, J. Valle) we further use this range of effective mass limits to construct a constraint on the mass  $m_{\min}$  of the lightest neutrino mass eigenstate, assuming the most disadvantageous combination of CP phases. This corresponds to  $m_{\min} < 0.69\text{--}1.63$  eV, in case neutrinos are Majorana particles.

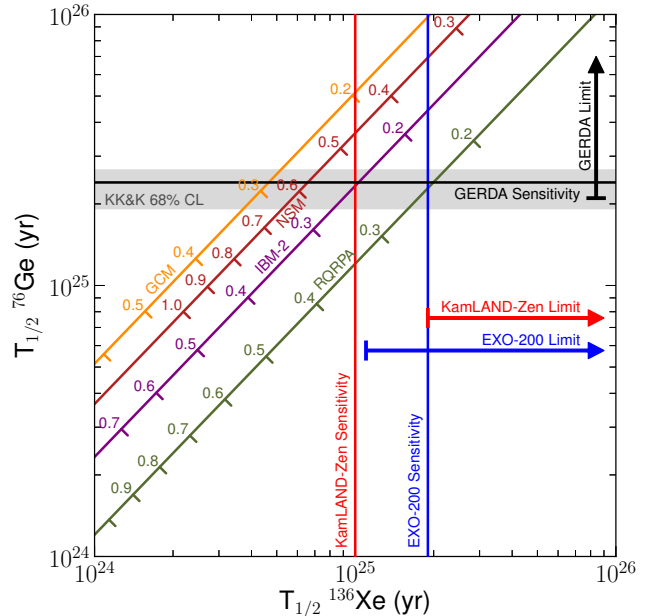


FIG. 6. **Comparison with recent results from  $^{136}\text{Xe}$  and  $^{76}\text{Ge}$   $0\nu\beta\beta$  experiments.** Sensitivity (orthogonal lines) and limits (arrows) from GERDA and KamLAND-Zen are from [11] and [12], respectively. The diagonal lines are derived from several recent nuclear matrix element calculations and the phase-space factor from [21], included to allow comparison between results from the two nuclei: GCM [28], NSM [29], IBM-2 [30], and RQRPA [31]. Tick marks along these lines indicate the associated effective neutrino mass in eV. The claimed observation in  $^{76}\text{Ge}$  (KK&K, [14]) is shown as a shaded gray band. The previous EXO-200 limit and sensitivity from [13] were  $1.6 \cdot 10^{25}$  yr and  $0.7 \cdot 10^{25}$  yr, respectively.

The results reported here supersede those of [13], owing to the increased exposure and improved analysis. The limit presented is however not as strong as the limit from [13], consistent with expected statistical fluctuations in the data. An appropriate metric to characterize the improvement of the experiment and independent of such fluctuations is the ‘sensitivity’, defined as the median expected 90% CL half-life limit assuming the background estimated from the ML fit and the absence of a  $0\nu\beta\beta$  signal. We calculate this metric using an ensemble of limits determined from Monte Carlo pseudo-experiments and find the EXO-200 sensitivity to be  $1.9 \cdot 10^{25}$  yr, representing a factor of 2.7 improvement in comparison to [13].

In Fig. 6 we compare the  $0\nu\beta\beta$  sensitivity and half-life limits from the GERDA, KamLAND-Zen, and EXO-200 experiments. Also shown is the positive observation claim in  $^{76}\text{Ge}$  from [14]. The results of the present analysis are inconsistent with the central value of this claim at 90% CL for two of the four considered nuclear matrix element calculations: GCM [28] and NSM [29].

The first two years of EXO-200 data demonstrate the power of a large and homogeneous LXe TPC in the search

for  $0\nu\beta\beta$ . Simulations of the nEXO experiment, a proposed 5000 kg LXe TPC based on the EXO-200 design, show that the state-of-the-art background measured in EXO-200 can be further improved by finer charge read-out pitch (to improve the SS/MS discrimination) and by lower electronic noise in the scintillation channel. In addition Xe self-shielding will become more powerful in larger detectors, where the  $\gamma$  attenuation length at energies near the Q-value becomes small with respect to the linear size of the LXe vessel. This advantage only applies to monolithic, homogeneous detectors.

## ACKNOWLEDGMENTS

EXO-200 is supported by DOE and NSF in the United States, NSERC in Canada, SNF in Switzerland, NRF in Korea, RFBR (12-02-12145) in Russia and DFG Cluster of Excellence “Universe” in Germany. EXO-200 data analysis and simulation uses resources of the National Energy Research Scientific Computing Center (NERSC), which is supported by the Office of Science of the U.S. Department of Energy under Contract No. DE-AC02-

05CH11231. The collaboration gratefully acknowledges the WIPP for their hospitality.

## VI. AUTHOR CONTRIBUTIONS

Each of the authors of this article participated in the collection and analysis of the data reported here, with the following exceptions: D. Beck has contributed to the slow controls system; G.F. Cao has performed energy resolution simulations; X.S. Jiang and Y.B. Zhao provide electronics expertise; M. Danilov, A. Dolgolenko, T. Koffas, and P. Vogel contributed to the initial conception and design of the experiment; M. Danilov and A. Dolgolenko also contributed to the acquisition of the xenon, while P. Vogel also advises on nuclear and particle theory; J. Davis, R. Nelson, and A. Rivas provide engineering, operations, and technical support at the WIPP facility; A. Johnson, J.J. Russell, and A. Waite support data acquisition, data processing, and software. Per collaboration policy, the authors are listed here alphabetically. EXO-200 was constructed and commissioned by the authors of Ref. [15, 33].

- 
- [1] E. Majorana, “Theory of the symmetry of electrons and positrons,” *Nuovo Cimento*, **14**, 171–184 (1937), no. 4.
  - [2] G. Racah, “On the symmetry of particles and antiparticles,” *Nuovo Cimento*, **14**, 322–328 (1937), no. 7.
  - [3] V. Mourik *et al.*, “Signatures of majorana fermions in hybrid superconductor-semiconductor nanowire devices,” *Science*, **336**, 1003–1007 (2012).
  - [4] L. Camilleri, E. Lisi, and J. F. Wilkerson, “Neutrino masses and mixings: Status and prospects,” *Annu. Rev. Nucl. Part. Sci.*, **58**, 343–369 (2008).
  - [5] R. N. Mohapatra and G. Senjanovic, “Neutrino mass and spontaneous parity violation,” *Phys. Rev. Lett.*, **44**, 912–915 (1980).
  - [6] M. Gell-Mann, P. Ramond, and R. Slansky, “Complex spinors and unified theories,” in *Supergravity*, edited by P. van Nieuwenhuizen and D. Freedman (North Holland Publishing Co, 1979) pp. 315–321, available arXiv:1306.4669.
  - [7] J. Schechter and J. Valle, “Neutrinoless double- $\beta$  decay in SU(2)  $\times$  U(1) theories,” *Phys. Rev. D*, **25**, 2951–2954 (1982).
  - [8] A. Barabash, “Precise half-life values for two-neutrino double- $\beta$  decay,” *Phys. Rev. C*, **81**, 035501 (2010).
  - [9] J. B. Albert *et al.* (EXO-200 Collaboration), “An improved measurement of the  $2\nu\beta\beta$  half-life of Xe-136 with EXO-200,” *Phys. Rev. C*, **89**, 015502 (2014).
  - [10] P. Vogel, “Nuclear structure and double beta decay,” *J. Phys. G: Nucl. Part. Phys.*, **39**, 124002 (2012).
  - [11] M. Agostini *et al.* (GERDA Collaboration), “Results on neutrinoless double- $\beta$  decay of  $^{76}\text{Ge}$  from Phase I of the GERDA experiment,” *Phys. Rev. Lett.*, **111**, 122503 (2013).
  - [12] A. Gando *et al.* (KamLAND-Zen Collaboration), “Limit on neutrinoless  $\beta\beta$  decay of  $^{136}\text{Xe}$  from the first phase of KamLAND-Zen and comparison with the positive claim in  $^{76}\text{Ge}$ ,” *Phys. Rev. Lett.*, **110**, 062502 (2013).
  - [13] M. Auger *et al.* (EXO-200 Collaboration), “Search for neutrinoless double-beta decay in  $^{136}\text{Xe}$  with EXO-200,” *Phys. Rev. Lett.*, **109**, 032505 (2012).
  - [14] H. Klapdor-Kleingrothaus and I. Krivosheina, “The evidence for the observation of  $0\nu\beta\beta$  decay: The identification of  $0\nu\beta\beta$  events from the full spectra,” *Mod. Phys. Lett. A*, **21**, 1547–1566 (2006).
  - [15] M. Auger *et al.*, “The EXO-200 detector, part I: Detector design and construction,” *JINST*, **7**, P05010 (2012).
  - [16] M. Redshaw, E. Wingfield, J. McDaniel, and E. G. Myers, “Mass and double-beta-decay Q value of  $^{136}\text{Xe}$ ,” *Phys. Rev. Lett.*, **98**, 053003 (2007).
  - [17] 3M HFE-7000, <http://www.3m.com>, (2014).
  - [18] E.-I. Esch *et al.*, “The cosmic ray muon flux at WIPP,” *Nucl. Inst. & Meth. A*, **538**, 516–525 (2005).
  - [19] D. Leonard *et al.*, “Systematic study of trace radioactive impurities in candidate construction materials for EXO-200,” *Nucl. Inst. & Meth. A*, **591**, 490–509 (2008).
  - [20] J. Allison *et al.*, “Geant4 developments and applications,” *IEEE Trans. Nucl. Sci.*, **53**, 270–278 (2006), ISSN 0018-9499.
  - [21] J. Kotila and F. Iachello, “Phase-space factors for double- $\beta$  decay,” *Phys. Rev. C*, **85**, 034316 (2012).
  - [22] G. Battistoni *et al.*, “The FLUKA code: description and benchmarking,” in *Hadronic Shower Simulation Workshop*, American Institute of Physics Conference Series, Vol. 896, edited by M. Albrow and R. Raja (2007) pp. 31–49.
  - [23] A. Ferrari, P. R. Sala, A. Fasso, and J. Ranft, *FLUKA: A multi-particle transport code (Program version 2005)*, Tech. Rep. CERN-2005-010, SLAC-R-773, INFN-TC-05-11 (CERN, 2005).



- [24] W. B. Wilson, *SOURCES 4A : a code for calculating ( $\alpha, n$ ) spontaneous fission, and delayed neutron sources and spectra*, Tech. Rep. LA-13639-MS (Los Alamos National Laboratory, Los Alamos, NM, USA, 1999).
- [25] M. Bhat, “Evaluated nuclear structure data file (ENSDF),” in *Nuclear Data for Science and Technology*, Research Reports in Physics, edited by S. Qaim (Springer Berlin Heidelberg, 1992) pp. 817–821, ISBN 978-3-642-63473-4.
- [26] S. S. Wilks, “The large-sample distribution of the likelihood ratio for testing composite hypotheses,” *Ann. Math. Statist.*, **9**, 60–62 (1938).
- [27] G. Cowan, *Statistical Data Analysis*, Oxford science publications (Clarendon Press, 1998).
- [28] T. R. Rodriguez and G. Martínez-Pinedo, “Energy density functional study of nuclear matrix elements for neutrinoless  $\beta\beta$  decay,” *Phys. Rev. Lett.*, **105**, 252503 (2010).
- [29] J. Menéndez, A. Poves, E. Caurier, and F. Nowacki, “Disassembling the nuclear matrix elements of the neutrinoless  $\beta\beta$  decay,” *Nucl. Phys. A*, **818**, 139–151 (2009).
- [30] J. Barea, J. Kotila, and F. Iachello, “Nuclear matrix elements for double- $\beta$  decay,” *Phys. Rev. C*, **87**, 014315 (2013).
- [31] F. Šimkovic, V. Rodin, A. Faessler, and P. Vogel, “ $0\nu\beta\beta$  and  $2\nu\beta\beta$  nuclear matrix elements, quasiparticle random-phase approximation, and isospin symmetry restoration,” *Phys. Rev. C*, **87**, 045501 (2013).
- [32] D. V. Forero, M. Tórtola, and J. W. F. Valle, “Global status of neutrino oscillation parameters after Neutrino-2012,” *Phys. Rev. D*, **86**, 073012 (2012).
- [33] N. Ackerman *et al.* (EXO-200 Collaboration), “Observation of two-neutrino double-beta decay in  $^{136}\text{Xe}$  with EXO-200,” *Phys. Rev. Lett.*, **107**, 212501 (2011).